ACS APPLIED MATERIALS & INTERFACES

Research Article

Cite This: ACS Appl. Mater. Interfaces 2018, 10, 38151−38158

www.acsami.org

Grain Boundary Softening: A Potential Mechanism for Lithium Metal Penetration through Stiff Solid Electrolytes

Seungho Yu[†] and Donald J. Siegel*[,†,‡,§,∥]

[†]Department of Mechanical Engineering, [‡]Department of Materials Science & Engineering, [§]Applied Physics Program, and [∥]University of Michigan Energy Institute, University of Michigan, 2350 Hayward Avenue, Ann Arbor, Michigan 48109, United States

Supporting Information

ABSTRACT: Models based on linear elasticity suggest that a solid electrolyte with a high shear modulus will suppress "dendrite" formation in batteries that use metallic lithium as the negative electrode. Nevertheless, recent experiments find that lithium can penetrate stiff solid electrolytes through microstructural features, such as grain boundaries. This failure mode emerges even in cases where the electrolyte has an average shear modulus that is an order of magnitude larger than that of Li. Adopting the solid-electrolyte $Li_7La_3Zr_2O_{12}$ (LLZO) as a prototype, here we demonstrate that significant softening in elastic properties occurs in nanoscale regions near grain boundaries. Molecular dynamics simulations performed on tilt and twist boundaries reveal that the grain boundary shear modulus is up to 50% smaller than in bulk regions. We propose that inhomogeneities in elastic properties arising from microstructural features provide a mechanism by which soft lithium can penetrate ostensibly stiff solid electrolytes.

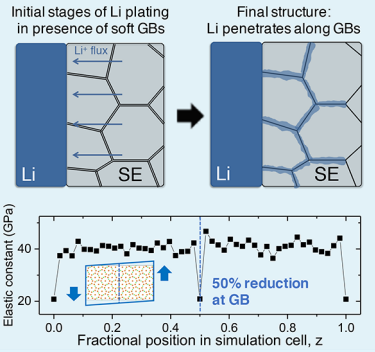

KEYWORDS: *solid electrolytes, grain boundaries, molecular dynamics, dendrites, energy storage, batteries*

INTRODUCTION

Batteries with energy densities beyond that of today's Li-ion systems are key to emerging applications that require enhanced energy storage.[1,2] The development of solid electrolytes (SEs) is one pathway for achieving these performance enhancements. For example, a solid-electrolyte-based cell would enable the substitution of a higher-capacity metallic Li anode in place of intercalated graphite[3−5] and improve the prospects for emerging chemistries, such as Li−S and Li−air.[6,7] Additionally, SEs can minimize safety concerns associated with the use of flammable and volatile organic liquid electrolytes.[4,8]

To be used in combination with a metallic Li negative electrode, a solid electrolyte should suppress the formation of Li "dendrites" during charging.[9−24] Dendrite formation can result in cell failure by creating an internal short circuit between the electrodes. Li metal cells based on liquid electrolytes are well known to undergo this failure mode;[25−28] hence, secondary batteries based on this (metal) electrode/(liquid) electrolyte combination have not been successfully commercialized.

Given the relative softness of Li metal,[29] it has been proposed that dendrite initiation can be prevented by pairing the Li anode with a stiff solid electrolyte.[30] Monroe and Newman used linear elasticity theory to examine the conditions under which a homogeneous polymer SE could suppress dendrite initiation.[31] Their model predicted that a SE whose shear modulus, G, was approximately twice larger (∼8 GPa) than that of Li metal[29] should prevent dendrite formation. Nevertheless, Li metal penetration has been recently reported in several SEs, such as β-Li_3PS_4,[10] $Li_2(OH)_{0.9}F_{0.1}Cl$,[16] and $Li_7La_3Zr_2O_{12}$ (LLZO).[9−15,17−19] This unexpected behavior occurred despite the fact that the measured densities and moduli for these materials were very high: in the case of LLZO, $G \sim 60$ GPa, which is more than an order of magnitude larger than that of Li metal, while the measured density was 98% of the theoretical value, indicating minimal contributions from porosity. Importantly, the metal penetrants were observed to follow pathways through the SE that coincided with the grain boundary (GB) network[9] or with the location of other microstructural features, such as pores or surface cracks.[10,32]

The penetration of stiff ceramic SEs by soft Li is a surprising observation and raises the question, "how is this possible?" Experimental data indicating contributions from the SE's grain boundaries, pores, and surface flaws lead us to hypothesize that *microstructural features* play a critical role in the suppression of dendrites. Existing models for dendrite nucleation in the presence of a SE do not account for microstructural inhomogeneities: the SE is typically assumed to be homogeneous.[21,31,33] Thus, a high shear modulus in the nondefective "bulk" regions of a SE may be considered as a necessary, but insufficient condition for achieving dendrite resistance: contributions from microstructure should also be considered.

Received: October 2, 2018
Accepted: October 12, 2018
Published: October 12, 2018

DOI: 10.1021/acsami.8b17223
ACS Appl. Mater. Interfaces 2018, 10, 38151−38158

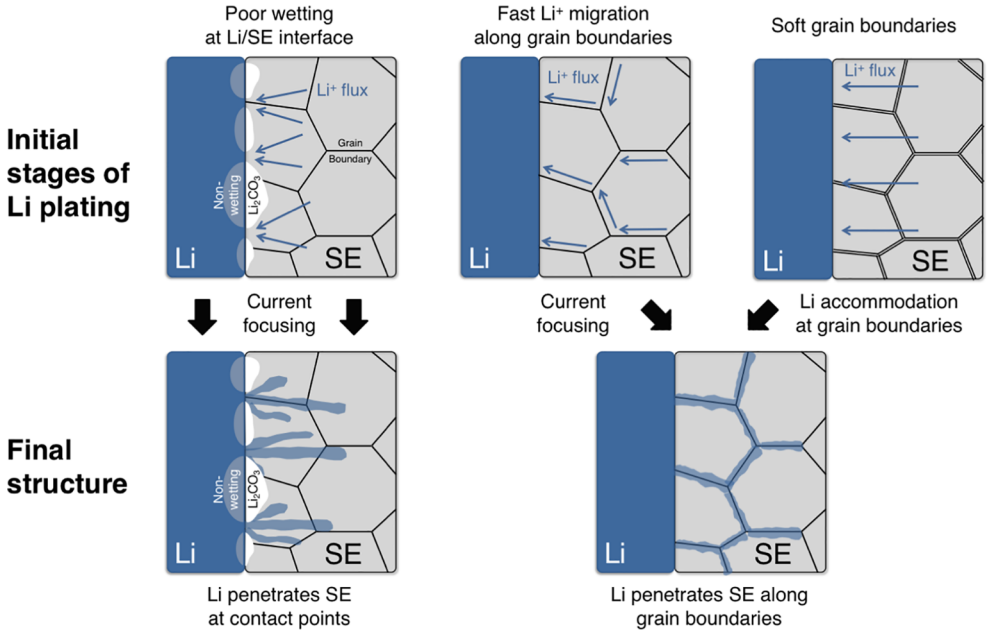

Figure 1. Potential microstructural contributions to inhomogeneous Li plating from a solid electrolyte (SE). Left and middle: current focusing mechanisms resulting from poor interfacial wetting or fast Li-ion migration along GBs. Right: accommodation of electrodeposited Li at soft GBs.

Figure 1 illustrates three scenarios by which microstructural features can promote inhomogeneous Li plating, resulting in metal penetration through a solid electrolyte (these scenarios do not represent an exhaustive list of possibilities; rather, these are the mechanisms that in our experience are important). The first scenario, shown on the left of Figure 1, arises from poor wetting at the Li/SE interface.[34−36] Taking LLZO as a prototype electrolyte, our earlier studies[35,37] have shown that Li metal will wet a "clean" LLZO surface; however, nonwetting behavior is observed when surface contaminant phases, such as LiOH and Li_2CO_3, are present. In addition, Li-ion transport through hydroxides and carbonates is slower than in LLZO. Thus, the presence of these contaminants results in focusing of Li ions away from regions containing carbonates/hydroxides and toward the (limited) contact points where the SE directly interfaces with the Li anode. This current focusing results in inhomogeneous electrodeposition of Li and ultimately to the penetration of Li metal into the SE. A similar mechanism has been proposed for the penetration of sodium metal through β''-Al_2O_3.[38] In the case of LLZO, cleaning of the SE surface was found to delay the onset of Li penetration to higher current densities.[35] Nevertheless, dendrites were still observed at current densities (0.6 mA/cm^2) far below those needed for a practical battery (3−10 mA/cm^2).[39] Thus, although increasing interfacial wetting is helpful, it appears to be insufficient on its own to eliminate the dendrite problem: other mechanisms appear to be contributing.

A second scenario resulting in dendrite formation is shown in the middle portion of Figure 1. This mechanism also involves current focusing and is caused by fast Li-ion migration along GBs. In the presence of fast GB transport, Li plating would occur preferentially in regions where GBs intersect the electrode surface. Assuming that the arrival rate of Li at these intersections is faster than its lateral migration away (i.e., parallel to the interface), then the resulting 'pile-up' of Li could nucleate dendrites. In prior work, we tested this "fast GB diffusion" hypothesis by calculating the rate of Li-ion migration along three low-energy GBs in LLZO.[40] Those and subsequent calculations in other SEs[41] found that GB transport was comparable to, or slower than, transport in the bulk. Thus, current focusing along GBs does not appear to explain Li dendrite penetration.

Here, we hypothesize that "softening" of the SE in the vicinity of GBs provides a mechanism for dendrite penetration. This hypothesis represents a third microstructure-related scenario and is shown on the right in Figure 1 (we speculated that GB softening could contribute to dendrite penetration in an earlier publication[42]). Here, "softening" is defined as a reduction in the elastic moduli close to the GBs. These effects could arise from deviations in density and atomic structure (i.e., less-optimal bonding relative to the bulk) near the GB plane. This scenario is inspired by the elasticity model of Monroe and Newman,[31] yet accounts for inhomogeneities in elastic properties. Unlike the first two scenarios from Figure 1, in which current focusing drives inhomogeneous Li deposition, in the present case Li deposition is initially homogeneous (i.e., the Li-ion current is *not* focused). However, as plating progresses, Li will accumulate preferentially in softer regions near electrode/GB junctions via interfacial diffusion away from the stiffer, GB-free regions. The resulting Li protrusions will generate locally stronger electric fields that will focus subsequent Li deposition. Indeed, prior studies have indicated the possibility of softening at GBs.[43,44] If these effects are also present in SEs, then they could provide an important contribution to the mechanism by which dendrites penetrate SEs.

The present study demonstrates that significant softening can occur at GBs in SEs. Adopting LLZO as a model SE, molecular dynamics (MD) simulations on two, low-energy $\sum 5$ tilt and twist GBs are reported. The elastic constants associated to uniaxial strain perpendicular to the GB plane and with shear parallel to the GB were calculated at 300 K. These calculations indicate a severe softening in the immediate vicinity of the GB: elastic constants are observed to be up to 50% smaller at GBs than in the bulk. We propose that nanoscale softening attributed to microstructural features, such as GBs, may

DOI: 10.1021/acsami.8b17223
ACS Appl. Mater. Interfaces 2018, 10, 38151−38158

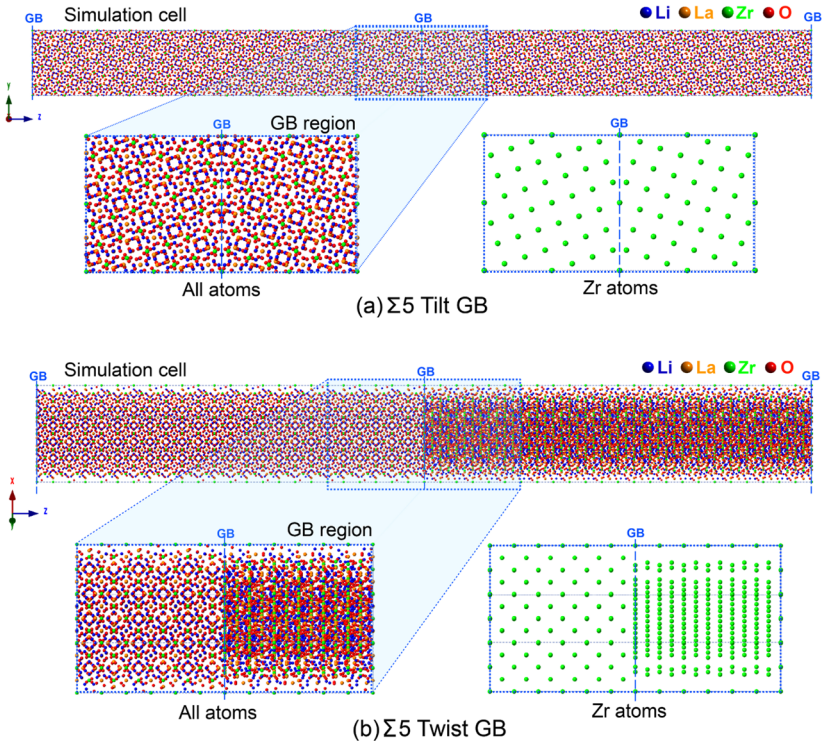

Figure 2. Computational models of (a) ∑5 tilt and (b) twist grain boundaries in LLZO. The full simulation cells and magnifications of one of the GB regions are shown in each case. GBs are located at $z = 0$ and $z = 0.5$ and denoted with the vertical dashed lines. The coincident site nature of the grains is illustrated by showing only the Zr sublattice sites.

Table 1. Calculated Elastic Constants, C_{ij}, and Moduli (GPa) for Cubic LLZO as a Function of Composition and Evaluation Method (DFT Calculations, MD Calculations, and Experimental Measurements)[a]

system	method	C_{11}	C_{12}	C_{44}	B	G	E
Al-doped LLZO	DFT (0 K)[b]	187	75	71	112	65	163
Al-doped LLZO	DFT (298 K)[b]					61	155
Al-doped LLZO	experiment (298 K)[b,c]				100.2, 102.8	58.1, 59.8, 59.6	146.1, 150.3, 149.8
Ta-doped LLZO	DFT (0 K)[b]	170	64	70	99	63	155
Ta-doped LLZO	DFT (298 K)[b]					59	147
Ta-doped LLZO	experiment (298 K)[b]				96.0	55.7, 61.2	139.9, 153.8
pure LLZO	DFT (0 K)[d]	186	78	73	114	65	163
pure LLZO	MD (0 K)[d,e]	190 (2%)	115 (47%)	29 (−60%)	140 (23%)	32 (−51%)	90 (−45%)
pure LLZO	MD (0 K)[d,f]	211 (13%)	95 (22%)	76 (4%)	134 (18%)	68 (5%)	175 (7%)
pure LLZO	MD (0 K)[d,g]	184 (−1%)	79 (1%)	60 (−18%)	114 (0%)	57 (−12%)	146 (−10%)

[a]The percent differences between DFT- and MD-predicted values for pure LLZO are given in parentheses. [b]Ref 29. [c]Ref 57. [d]Present study. [e]The softBV force field by Adams et al. is based on a Morse-type interaction derived from bond valence parameters and Coulombic repulsion, ref 54. [f]Force fields from ref 55 (Klenk et al.), consisting of a long-range Coulombic interaction and a short-ranged Buckingham interaction. [g]Force field from ref 56 (Jalem et al.), consisting of a long-range Coulombic interaction and a short-ranged Buckingham interaction.

explain *why* these features are susceptible to metal penetration during electrodeposition.

METHODOLOGY

Calculations were performed on the high-conductivity cubic polymorph of LLZO.[45,46] Li was distributed on the 24d and 96h sites with occupancies of 0.543 and 0.448, respectively, as described in earlier studies.[29,37] Elastic properties were evaluated at a pair of low-energy tilt and twist coincident site (∑5) GBs, shown in Figure 2. The procedure for constructing these GBs is shown in Figure S1. GB models were generated by initially rotating two replicas of the unit LLZO cell (i.e., the individual grains) along their [001] axes by 53.1° (relative displacement). Overlaying the rotated grains results in the formation of a coincident cite lattice where 1 in 5 Zr sites overlap, thus the designation "∑5" is commonly used. The symmetric tilt GB was constructed by cleaving and then adjoining the rotated grains along their (210) planes. This GB was adopted in our prior study of Li-ion diffusion at GBs in LLZO.[40] Similarly, the twist boundary was formed by cleaving and adjoining the rotated grains along (001) planes.

At present, the detailed distribution of GB structures in LLZO is not known. Nevertheless, the low energies of the two GB orientations[47,48] examined here suggest that they are likely to be present in equilibrated LLZO samples.[40,49] Earlier studies have shown that coincident site (∑5) GBs in body-centered cubic materials exhibit low energies (the Zr sublattice in LLZO is BCC),[47,48] whereas in oxides low-energy GBs exhibit habit planes that are constructed from the same planes as those that

DOI: 10.1021/acsami.8b17223
ACS Appl. Mater. Interfaces 2018, 10, 38151−38158

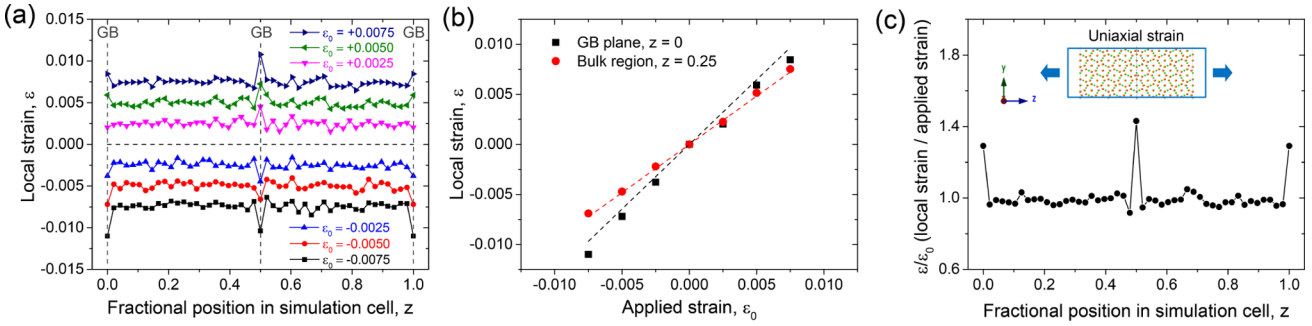

Figure 3. Calculated local strains for the ∑5 tilt GB cell at 300 K under uniaxial loading. (a) Local strain as a function of position normal to the GB plane; (b) relation between local and applied (global) strain in the GB plane at $z = 0$ and in the bulk region ($z = 0.25$); (c) ratio of local to applied strain as a function of position normal to the GB plane.

minimize the surface energy.[50] The ∑5(210) tilt boundary adopted here satisfies the first requirement (i.e., a misorientation angle allowing for a coincident site GB), whereas the ∑5(100) twist boundary satisfies both the orientation and surface energy requirement[51] (the (100) twist boundary plane was previously identified to be low in energy).[51,52]

Figure 2 illustrates the computational cells used to model these two GBs. In both cases, the cells contain a pair of GBs: one at the cell center (fractional coordinate $z = 0.5$) and one at the cell boundary ($z = 0$). The GB planes have normal vectors that are parallel to the long (z) direction of the cell, allowing for ample space (>15 nm) and minimum interaction between GBs. Alternative views of the simulation cells are shown in Figure S2. The cell dimensions and number of atoms they contain (~23 000) are listed in Table S1.

The elastic properties of bulk LLZO and of the two GBs were evaluated using molecular dynamics (MD) simulations, as implemented in the LAMMPS code.[53] The time step for all MD runs was 2 fs. Three force fields (FFs)[54−56] were assessed with respect to their ability to reproduce the bulk elastic properties of LLZO, as previously predicted by first-principles calculations and as measured by experiments.[29,57] In an earlier study, we reported that the DFT-calculated elastic properties were in excellent agreement to experimental measurements for Ta- and Al-doped LLZO.[29]

Table 1 compares the 0 K and room-temperature elastic constants and moduli for bulk LLZO, as calculated using MD, with DFT and experimental data.[58] Out of the three FFs, the potential of Jalem and co-workers[56] yielded the best agreement with the elastic constants predicted by DFT, with a mean absolute deviation of 7%. This interatomic potential was adopted for calculations on GB cells. It is based on long-range Coulombic and a short-ranged Buckingham interaction; the cutoff distance for the short-range interaction was set to 10.5 Å.

The equilibrium structure and composition of the GBs was determined using a multistep procedure similar to that employed in our earlier analysis of GB transport, Figure S3.[40] After an initial geometry optimization at 0 K, the simulation cells were equilibrated using NPT-MD at 300 K for 500 ps. Subsequently, they were heated to 1000 K at a rate of 1 K/ps using the NPT ensemble. This procedure accommodates thermal expansion and volume changes associated with the presence of the GBs. Upon reaching 1000 K, isothermal MD was performed in the NPT and (subsequently) NVT ensembles for 500 ps each. Next, to equilibrate the local composition of the GBs, NVT Monte Carlo simulations were performed (10^6 attempts) using the Metropolis algorithm[59] with a maximum atomic displacement of 0.5 Å. The cells were then cooled to 300 K via MD at a rate of 1 K/ps and equilibrated at 300 K for 500 ps using NPT-MD with a constant cell shape to suppress the phase transform to the low-conductivity tetragonal phase. Finally, NVT-MD was performed at 300 K for 500 ps.

GB elastic properties were calculated using the methodology described for twist GBs in copper.[43,44] A series of uniaxial or shear strains of magnitudes −0.75%, −0.5%, −0.25%, 0.25%, 0.5%, and 0.75% were applied to the boundary of the simulation cell (in one instance of shearing the twist GB, application of the −0.75% strain appeared to result in plastic deformation; in this case, data from that strain configuration were not used). The stress associated to a given applied strain was obtained from the appropriate time-averaged component of the pressure tensor. These components were derived from the kinetic energy and virial tensors and were averaged over a 400 ps window of molecular dynamics using a 1 ps sampling rate.[53] These global strains generate localized uniaxial strains perpendicular to the GB plane and shear strain parallel to the GB plane, respectively. Local strains were evaluated as a function of position in the computational cell by measuring the relative positions of planes of La and Zr atoms. For the tilt (twist) GB, the unstrained interplanar spacing, $L_{z,0}$, is given by $\sqrt{5}a/4$ ($a/2$), where a is the lattice constant of the cubic unit cell, Figure S4.

The elastic constant, C_{33}, is associated to uniaxial strain perpendicular to the GB plane (z-direction). Changes to the interplanar spacing perpendicular to the GB plane were used to measure local deformations resulting from the global strain, $\varepsilon_{33,0}$. The local uniaxial strain, ε_{33}, is given by $\varepsilon_{33} = (L_z - L_{z,0})/L_{z,0}$ where $L_{z,0}$ and L_z are, respectively, the interplanar spacings before and after strain is applied. The local elastic constant is then given by: $C_{33} = \sigma_{33}/\varepsilon_{33}$, where σ_{33} is the global stress in the z-direction.

The elastic constant associated to shear parallel to the GB plane, C_{44}, was calculated by applying a shear strain, $\varepsilon_{44,0}$, to the simulation cell in the y-direction. The local shear strain, ε_{44}, can be expressed as: $\varepsilon_{44} = \Delta d_{Ly}/L_{z,0}$. Here, $L_{z,0}$ is the interplanar spacing along the z-direction of a given region in the cell before strain is applied, whereas Δd_{Ly} represents the magnitude of displacement in the direction of the shear (the y-direction in our calculations) across that region. These displacements were measured by tracking the y-components of atom positions on the two planes that bound a given region in the z-direction. The local elastic constant is then given by

DOI: 10.1021/acsami.8b17223
ACS Appl. Mater. Interfaces 2018, 10, 38151−38158

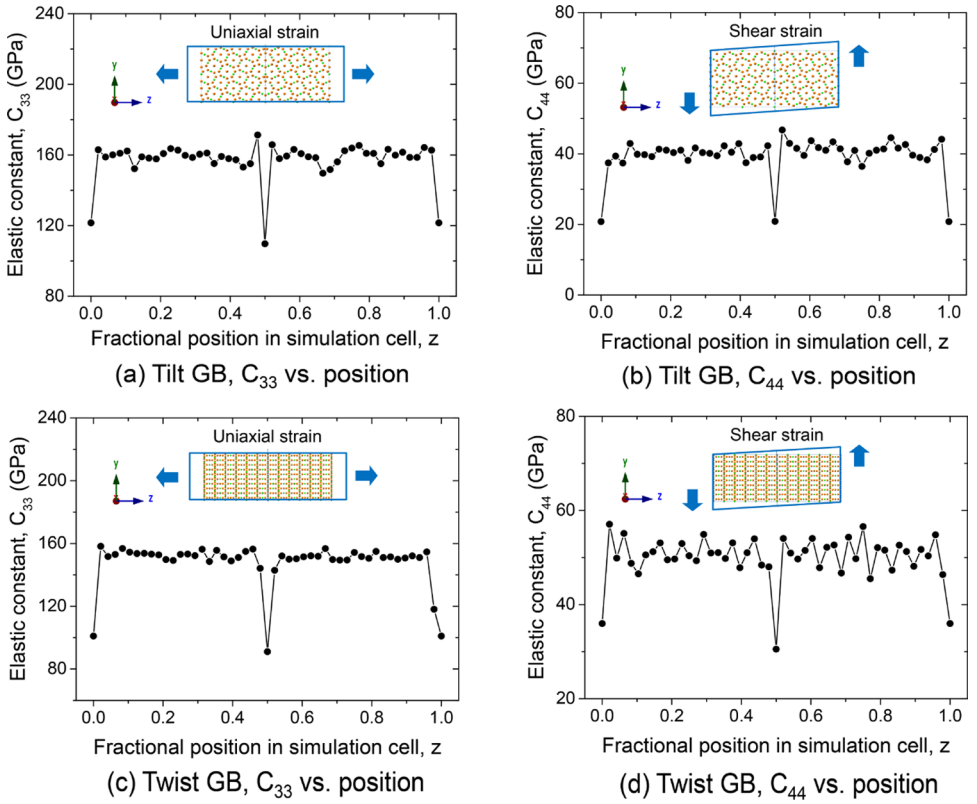

Figure 4. Calculated elastic constants C_{33} and C_{44} at 300 K as a function of position normal to the GB planes for the (a, b) the ∑5 symmetric tilt GB cell and (c, d) the ∑5 twist GB cell.

$C_{44} = \sigma_{44}/\varepsilon_{44}$, where σ_{44} is the global shear stress. See Figure S5 for additional details.

RESULTS AND DISCUSSION

GBs in LLZO have been reported to introduce excess volume into the lattice.[40] The calculated excess volumes for the tilt and twist GBs at 300 K examined here are 623 and 520 Å^3, corresponding to 0.24% and 0.2% increases in the cell volume, or a linear expansion normal to the GB plane of 0.42 and 0.31 Å per GB, respectively. The corresponding GB energies are 0.75 and 0.83 J/m^2. In agreement to our previous study,[40] the composition near the tilt GB is slightly enriched with lithium and oxygen. The Li^+ enrichment within the GB plane at least partially results from a redistribution of Li^+ from the planes immediately adjacent to the GB. In contrast, at the twist GB a depletion of oxygen, La, and Zr is observed. Local composition data for both GB models are shown in Figure S6.

Figure 3 shows the calculated strain behavior of the ∑5 tilt GB cell under uniaxial loading at 300 K. Figure 3a presents the local strain as a function of the global applied strain and of position normal to the GB plane. As expected, the local strain in the bulk region is very similar to the global strain. In contrast, the local strain in the immediate vicinity of the GB is much larger than in the bulk, suggesting a softening in the GB region. Figure 3b shows that the relationships between the local and global applied strain in the bulk and GB regions are in both cases roughly linear for the strains examined here. Although the slope of the line fit to the bulk data is approximately unity, for the GB the slope is ∼30% steeper, consistent again with GB softening. Finally, Figure 3c plots the ratio of local to global strain, $\varepsilon/\varepsilon_0$, as a function of position normal to the GB plane. These data were obtained from the slopes of linear fits to the position-dependent local strain (as in Figure 3b). Factoring in both GBs, Figure 3c shows that the strain in the GB region is ∼40% greater than that of the bulk. The calculated strain response of the tilt GB to a shear load is shown in Figure S7. Similar data for the twist GB are given in Figures S8 and S9. In all cases, the calculations predict that the magnitude of the local strain in the GB region exceeds that of the bulk.

Figure 4 plots the elastic constants C_{33} and C_{44} for the tilt and twist GBs as a function of position normal to the GB plane. As previously described, these two elastic constants represent the elastic and shear modulus of the system: $C_{33} \sim E$ and $C_{44} \sim G$. The elastic constant data were calculated by combining strain data from Figures 3 and S6-S8 with the stress for a given applied strain. A summary of all elastic constants is given in Table 2.

Turning first to the elastic constant associated with uniaxial strain, C_{33}, Figure 4a,c shows that C_{33} is approximately constant in the bulk regions of the computational cells and is equal to 159 and 152 GPa. This elastic constant is predicted to

Table 2. Calculated Elastic Constants, C_{33} and C_{44} (in GPa), in the Bulk and GB Regions for the ∑5 Tilt and Twist GB Simulation Cells[a]

	∑5 tilt GB			∑5 twist GB		
elastic constant	bulk	GB	Δ (%)	bulk	GB	Δ (%)
C_{33}, uniaxial	159	115	−28	152	96	−37
C_{44}, shear	40	21	−48	51	33	−35

[a]Δ gives the percentage change in a given elastic constant at the GB relative to the bulk region.

DOI: 10.1021/acsami.8b17223
ACS Appl. Mater. Interfaces 2018, 10, 38151−38158

be much smaller in the GB regions: a value of 115 GPa is obtained for the tilt GB, with an even smaller value of 96 GPa predicted for the twist system. These values are 28 and 37% smaller than the corresponding bulk values.

Similarly, the elastic constant associated with shear deformation, C_{44}, is predicted to be significantly smaller in both classes of GBs: in the bulk, C_{44} = 40 and 51 GPa, whereas in the tilt and twist GBs values of 21 and 33 GPa are found, respectively. Thus, the GBs are 48 and 35% softer with respect to shear than is the bulk. In total, our calculations predict that GBs in LLZO can have elastic moduli that are approximately 25−50% smaller than the bulk.

The softening at GBs observed here can result from several mechanisms. First, as previously mentioned, these GBs exhibit an excess free volume and thus a lower density compared to the bulk. Second, the composition near the GBs is predicted to differ from that of the bulk, as shown in Figure S6. Finally, the different atomic structure of the GB could result in a distinct bonding environment. Unfortunately, the classical interatomic potentials used in our calculations provide no information regarding the electronic structure and thus a detailed bonding analysis is not possible. Accessing this information will require a first-principles calculation; such a calculation is nontrival due to the large size of the computational cell.

Could GB "soft spots" explain Li metal penetration in LLZO? A strict interpretation of the Monroe−Newman criterion stipulates that a viable SE should have a shear modulus, G, that is approximately twice that of Li metal. Assuming Li can be treated as an isotropic polycrystalline metal, then $G_{Li} \sim 4$ GPa.[29] Thus, a solid electrolyte with $G_{SE} > \sim 8$ GPa $= 2G_{Li}$ should be capable of suppressing dendrite initiation. Even though our calculations predict that GBs in LLZO are up to ∼50% softer than the bulk, the smallest value for C_{44} obtained for the GBs examined here, 21 GPa, easily surpasses the $2G_{Li}$ threshold. Therefore, it would seem that GBs, although significantly softer than the bulk, are not "soft enough" to serve as initiation points for dendrites.

A few caveats to this conclusion should be acknowledged, however. First, treating the Li anode as an isotropic solid may be overly simplistic. For example, our prior study reported that the elastic properties of Li are highly anisotropic:[29] the resolved shear modulus of Li ranges from a minimum of 1.5 GPa in the ⟨111⟩ direction to a maximum of approximately 11 GPa along ⟨100⟩.[29] Doubling the largest of these values results in a threshold of 22 GPa, a value which is larger than the shear modulus predicted for the ∑5 tilt boundary, 21 GPa. Hence, this GB does not meet the Monroe−Newman criterion.

Second, as mentioned earlier, the atomic-scale structure and orientation distribution of GBs in LLZO are at present unknown. The low energies of the two GB orientations[47,48,50] examined here suggest that they are plausible structures in equilibrated LLZO samples, such as those processed using at high temperatures.[40,49] Nevertheless, the present GBs represent idealized systems with relatively low degrees of disorder and excess volume. It is therefore possible that they represent a best-case scenario: softening in less-ordered, general GBs could be more severe and extend to larger spatial regions. Higher energy GBs with less-compact structures could be generated via lower temperature synthesis routes. Solute segregation and impurity phases at GBs,[35,37,60−67] such as hydroxides and carbonates, could also impact elastic properties. Further study is needed to assess these factors.

Third, although softening is demonstrated here for GBs, it is reasonable to speculate that this behavior could also apply to other microstructural features that exhibit local disruptions to crystallinity and/or density, such as at surface scratches or near pores.[10,32]

Finally, given that real electrode/electrolyte interfaces are often structurally and compositionally complex, it is reasonable to consider whether the Monroe and Newman criterion (i.e., $\sim 2G_{Li}$) should be interpreted quantitatively or instead is best employed as a qualitative guideline. The latter interpretation suggests that local decreases in elastic properties, such as those caused by microstructural features, could be sufficient to promote metal penetration even if the local modulus is larger than $2G_{Li}$.

CONCLUSIONS

Inhomogeneities in the elastic response of a solid electrolyte were examined in the context of Monroe and Newman's elasticity model for dendrite initiation. Molecular dynamics simulations were used to evaluate elastic moduli near grain boundaries in the prototype solid electrolyte, LLZO. These calculations reveal that moduli can be as much as 50% smaller at grain boundaries than in the bulk. This inhomogeneous softening is expected to result in accumulation of Li at electrode/grain boundary junctions during electrodeposition. Thus, grain boundary "soft spots" may contribute to the mechanism by which soft lithium metal can penetrate an ostensibly stiff solid electrolyte. Additional study is needed to characterize the elastic properties of other types of grain boundaries, account for potential variations in grain boundary composition arising from impurities or segregation, and to explore effects in solids beyond LLZO.

This work highlights scenarios by which a solid electrolyte's microstructure can contribute to inhomogeneous electrodeposition and dendrite penetration. At present, these scenarios have received limited attention in the battery literature. A better understanding of the role of microstructure will aid in the design of long-lived solid-state batteries.

ASSOCIATED CONTENT

Supporting Information

The Supporting Information is available free of charge on the ACS Publications website at DOI: 10.1021/acsami.8b17223.

Details of simulation cells, computational procedure, grain boundary composition plots, and local strain and elastic constants for tilt and twist GBs (PDF)

AUTHOR INFORMATION

Corresponding Author

*E-mail: djsiege@umich.edu.

ORCID

Seungho Yu: 0000-0003-3912-6463

Donald J. Siegel: 0000-0001-7913-2513

Notes

The authors declare no competing financial interest.

ACKNOWLEDGMENTS

S.Y. and D.J.S. acknowledge financial support from the US Department of Energy, Advanced Research Projects Agency − Energy, grant no. DE-AR0000653. S.Y. also acknowledges support from the Kwanjeong Educational Foundation. D.J.S.

DOI: 10.1021/acsami.8b17223
ACS Appl. Mater. Interfaces 2018, 10, 38151−38158

acknowledges helpful discussions with J. Sakamoto, J. Wolfenstine, and N. Dasgupta.

REFERENCES

(1) Bruce, P. G.; Freunberger, S. A.; Hardwick, L. J.; Tarascon, J.-M. Li-O_2 and Li-S Batteries with High Energy Storage. *Nat. Mater.* **2012**, *11*, 19−29.

(2) Larcher, D.; Tarascon, J. M. Towards Greener and more Sustainable Batteries for Electrical Energy Storage. *Nat. Chem.* **2015**, *7*, 19.

(3) Li, J.; Ma, C.; Chi, M.; Liang, C.; Dudney, N. J. Solid Electrolyte: the Key for High-Voltage Lithium Batteries. *Adv. Energy Mater.* **2015**, *5*, No. 1401408.

(4) Goodenough, J. B.; Kim, Y. Challenges for Rechargeable Li Batteries. *Chem. Mater.* **2010**, *22*, 587−603.

(5) Luntz, A. C.; Voss, J.; Reuter, K. Interfacial Challenges in Solid-State Li Ion Batteries. *J. Phys. Chem. Lett.* **2015**, *6*, 4599−4604.

(6) Liu, Y.; He, P.; Zhou, H. Rechargeable Solid-State Li−Air and Li−S Batteries: Materials, Construction, and Challenges. *Adv. Energy Mater.* **2018**, *8*, No. 1701602.

(7) Yang, C.; Fu, K.; Zhang, Y.; Hitz, E.; Hu, L. Protected Lithium-Metal Anodes in Batteries: From Liquid to Solid. *Adv. Mater.* **2017**, *29*, No. 1701169.

(8) Roth, E. P.; Orendorff, C. J. How Electrolytes Influence Battery Safety. *Electrochem. Soc. Interface* **2012**, *21*, 45−49.

(9) Cheng, E. J.; Sharafi, A.; Sakamoto, J. Intergranular Li Metal Propagation through Polycrystalline $Li_{6.25}Al_{0.25}La_3Zr_2O_{12}$ Ceramic Electrolyte. *Electrochim. Acta* **2017**, *223*, 85−91.

(10) Porz, L.; Swamy, T.; Sheldon, B. W.; Rettenwander, D.; Frömling, T.; Thaman, H. L.; Berendts, S.; Uecker, R.; Carter, W. C.; Chiang, Y.-M. Mechanism of Lithium Metal Penetration through Inorganic Solid Electrolytes. *Adv. Energy Mater.* **2017**, *7*, No. 1701003.

(11) Tsai, C.-L.; Roddatis, V.; Chandran, C. V.; Ma, Q.; Uhlenbruck, S.; Bram, M.; Heitjans, P.; Guillon, O. $Li_7La_3Zr_2O_{12}$ Interface Modification for Li Dendrite Prevention. *ACS Appl. Mater. Interfaces* **2016**, *8*, 10617−10626.

(12) Ren, Y.; Shen, Y.; Lin, Y.; Nan, C.-W. Direct Observation of Lithium Dendrites inside Garnet-type Lithium-ion Solid Electrolyte. *Electrochem. commun.* **2015**, *57*, 27−30.

(13) Aguesse, F.; Manalastas, W.; Buannic, L.; Lopez del Amo, J. M.; Singh, G.; Llordés, A.; Kilner, J. Investigating the Dendritic Growth during Full Cell Cycling of Garnet Electrolyte in Direct Contact with Li Metal. *ACS Appl. Mater. Interfaces* **2017**, *9*, 3808−3816.

(14) Suzuki, Y.; Kami, K.; Watanabe, K.; Watanabe, A.; Saito, N.; Ohnishi, T.; Takada, K.; Sudo, R.; Imanishi, N. Transparent cubic garnet-type solid electrolyte of Al_2O_3-doped $Li_7La_3Zr_2O_{12}$. *Solid State Ionics* **2015**, *278*, 172−176.

(15) Sudo, R.; Nakata, Y.; Ishiguro, K.; Matsui, M.; Hirano, A.; Takeda, Y.; Yamamoto, O.; Imanishi, N. Interface behavior between garnet-type lithium-conducting solid electrolyte and lithium metal. *Solid State Ionics* **2014**, *262*, 151−154.

(16) Li, Y.; Zhou, W.; Chen, X.; Lü, X.; Cui, Z.; Xin, S.; Xue, L.; Jia, Q.; Goodenough, J. B. Mastering the interface for advanced all-solid-state lithium rechargeable batteries. *Proc. Natl. Acad. Sci. USA* **2016**, *113*, 13313.

(17) Hongahally Basappa, R.; Ito, T.; Morimura, T.; Bekarevich, R.; Mitsuishi, K.; Yamada, H. Grain Boundary Modification to Suppress Lithium Penetration through Garnet-Type Solid Electrolyte. *J. Power Sources* **2017**, *363*, 145−152.

(18) Wang, C.; Gong, Y.; Dai, J.; Zhang, L.; Xie, H.; Pastel, G.; Liu, B.; Wachsman, E.; Wang, H.; Hu, L. In Situ Neutron Depth Profiling of Lithium Metal−Garnet Interfaces for Solid State Batteries. *J. Am. Chem. Soc.* **2017**, *139*, 14257−14264.

(19) Cheng, L.; Chen, W.; Kunz, M.; Persson, K.; Tamura, N.; Chen, G.; Doeff, M. Effect of Surface Microstructure on Electrochemical Performance of Garnet Solid Electrolytes. *ACS Appl. Mater. Interfaces* **2015**, *7*, 2073−2081.

(20) Ma, J.; Chen, B.; Wang, L.; Cui, G. Progress and prospect on failure mechanisms of solid-state lithium batteries. *J. Power Sources* **2018**, *392*, 94−115.

(21) Barai, P.; Higa, K.; Srinivasan, V. Effect of Initial State of Lithium on the Propensity for Dendrite Formation: A Theoretical Study. *J. Electrochem. Soc.* **2017**, *164*, A180−A189.

(22) Tikekar, M. D.; Choudhury, S.; Tu, Z.; Archer, L. A. Design principles for electrolytes and interfaces for stable lithium-metal batteries. *Nat. Energy* **2016**, *1*, No. 16114.

(23) Chen, Q.; Geng, K.; Sieradzki, K. Prospects for Dendrite-Free Cycling of Li Metal Batteries. *J. Electrochem. Soc.* **2015**, *162*, A2004−A2007.

(24) Harry, K. J.; Hallinan, D. T.; Parkinson, D. Y.; MacDowell, A. A.; Balsara, N. P. Detection of subsurface structures underneath dendrites formed on cycled lithium metal electrodes. *Nat. Mater.* **2013**, *13*, 69.

(25) Wood, K. N.; Kazyak, E.; Chadwick, A. F.; Chen, K.-H.; Zhang, J.-G.; Thornton, K.; Dasgupta, N. P. Dendrites and Pits: Untangling the Complex Behavior of Lithium Metal Anodes through Operando Video Microscopy. *ACS Cent. Sci.* **2016**, *2*, 790−801.

(26) Aurbach, D. Review of selected electrode−solution interactions which determine the performance of Li and Li ion batteries. *J. Power Sources* **2000**, *89*, 206−218.

(27) Wandt, J.; Marino, C.; Gasteiger, H. A.; Jakes, P.; Eichel, R.-A.; Granwehr, J. Operando electron paramagnetic resonance spectroscopy - formation of mossy lithium on lithium anodes during charge-discharge cycling. *Energy Environ. Sci.* **2015**, *8*, 1358−1367.

(28) Bai, P.; Li, J.; Brushett, F. R.; Bazant, M. Z. Transition of lithium growth mechanisms in liquid electrolytes. *Energy Environ. Sci.* **2016**, *9*, 3221−3229.

(29) Yu, S.; Schmidt, R. D.; Garcia-Mendez, R.; Herbert, E.; Dudney, N. J.; Wolfenstine, J. B.; Sakamoto, J.; Siegel, D. J. Elastic Properties of the Solid Electrolyte $Li_7La_3Zr_2O_{12}$ (LLZO). *Chem. Mater.* **2016**, *28*, 197−206.

(30) Sundström, L.-G.; Bark, F. H. On morphological instability during electrodeposition with a stagnant binary electrolyte. *Electrochim. Acta* **1995**, *40*, 599−614.

(31) Monroe, C.; Newman, J. The Impact of Elastic Deformation on Deposition Kinetics at Lithium/Polymer Interfaces. *J. Electrochem. Soc.* **2005**, *152*, A396−A404.

(32) Wu, B.; Wang, S.; Lochala, J.; Desrochers, D.; Liu, B.; Zhang, W.; Yang, J.; Xiao, J. The role of the solid electrolyte interphase layer in preventing Li dendrite growth in solid-state batteries. *Energy Environ. Sci.* **2018**, *11*, 1803−1810.

(33) Tikekar, M. D.; Archer, L. A.; Koch, D. L. Stabilizing electrodeposition in elastic solid electrolytes containing immobilized anions. *Sci. Adv.* **2016**, *2*, No. e1600320.

(34) Zhou, W.; Li, Y.; Xin, S.; Goodenough, J. B. Rechargeable Sodium All-Solid-State Battery. *ACS Cent. Sci.* **2017**, *3*, 52−57.

(35) Sharafi, A.; Kazyak, E.; Davis, A. L.; Yu, S.; Thompson, T.; Siegel, D. J.; Dasgupta, N. P.; Sakamoto, J. Surface Chemistry Mechanism of Ultra-Low Interfacial Resistance in the Solid-State Electrolyte $Li_7La_3Zr_2O_{12}$. *Chem. Mater.* **2017**, *29*, 7961−7968.

(36) Han, X.; Gong, Y.; Fu, K.; He, X.; Hitz, G. T.; Dai, J.; Pearse, A.; Liu, B.; Wang, H.; Rubloff, G.; Mo, Y.; Thangadurai, V.; Wachsman, E. D.; Hu, L. Negating interfacial impedance in garnet-based solid-state Li metal batteries. *Nat. Mater.* **2017**, *16*, 572−579.

(37) Sharafi, A.; Yu, S.; Naguib, M.; Lee, M.; Ma, C.; Meyer, H. M.; Nanda, J.; Chi, M.; Siegel, D. J.; Sakamoto, J. Impact of Air Exposure and Surface Chemistry on Li-$Li_7La_3Zr_2O_{12}$ Interfacial Resistance. *J. Mater. Chem. A* **2017**, *5*, 13475−13487.

(38) Virkar, A. V.; Viswanathan, L.; Biswas, D. R. On the deterioration of ß″-alumina ceramics under electrolytic conditions. *J. Mater. Sci.* **1980**, *15*, 302−308.

(39) Albertus, P.; Babinec, S.; Litzelman, S.; Newman, A. Status and challenges in enabling the lithium metal electrode for high-energy and low-cost rechargeable batteries. *Nat. Energy* **2018**, *3*, 16−21.

DOI: 10.1021/acsami.8b17223
ACS Appl. Mater. Interfaces 2018, 10, 38151−38158

(40) Yu, S.; Siegel, D. J. Grain Boundary Contributions to Li-Ion Transport in the Solid Electrolyte $Li_7La_3Zr_2O_{12}$(LLZO). *Chem. Mater.* **2017**, *29*, 9639−9647.
(41) Dawson, J. A.; Canepa, P.; Famprikis, T.; Masquelier, C.; Islam, M. S. Atomic-Scale Influence of Grain Boundaries on Li-Ion Conduction in Solid Electrolytes for All-Solid-State Batteries. *J. Am. Chem. Soc.* **2018**, *140*, 362−368.
(42) Wolfenstine, J.; Allen, J. L.; Sakamoto, J.; Siegel, D. J.; Choe, H. Mechanical behavior of Li-ion-conducting crystalline oxide-based solid electrolytes: a brief review. *Ionics* **2018**, *24*, 1271−1276.
(43) Adams, J. B.; Wolfer, W. G.; Foiles, S. M. Elastic Properties of Grain Boundaries in Coopper and their Relationship to Bulk Elastic Constants. *Phys. Rev. B* **1989**, *40*, 9479−9484.
(44) Nomura, M.; Adams, J. B. Mechanical Properties of Twist Grain Boundaries in Cu. *Interface Sci.* **1994**, *2*, 137−146.
(45) Xie, H.; Alonso, J. A.; Li, Y.; Fernández-Díaz, M. T.; Goodenough, J. B. Lithium Distribution in Aluminum-Free Cubic $Li_7La_3Zr_2O_{12}$. *Chem. Mater.* **2011**, *23*, 3587−3589.
(46) Awaka, J.; Kijima, N.; Hayakawa, H.; Akimoto, J. Synthesis and Structure Analysis of Tetragonal $Li_7La_3Zr_2O_{12}$ with the Garnet-Related Type Structure. *J. Solid State Chem.* **2009**, *182*, 2046−2052.
(47) Tschopp, M. A.; Solanki, K. N.; Gao, F.; Sun, X.; Khaleel, M. A.; Horstemeyer, M. F. Probing Grain Boundary Sink Strength at the Nanoscale: Energetics and Length Scales of Vacancy and Interstitial Absorption by Grain Boundaries in alpha-Fe. *Phys. Rev. B* **2012**, *85*, No. 064108.
(48) Rajagopalan, M.; Tschopp, M. A.; Solanki, K. N. Grain Boundary Segregation of Interstitial and Substitutional Impurity Atoms in Alpha-Iron. *J. Mater.* **2014**, *66*, 129−138.
(49) David, I. N.; Thompson, T.; Wolfenstine, J.; Allen, J. L.; Sakamoto, J. Microstructure and Li-Ion Conductivity of Hot-Pressed Cubic $Li_7La_3Zr_2O_{12}$. *J. Am. Ceram. Soc.* **2015**, *98*, 1209−1214.
(50) Saylor, D. M.; Dasher, B.; Pang, Y.; Miller, H. M.; Wynblatt, P.; Rollett, A. D.; Rohrer, G. S. Habits of Grains in Dense Polycrystalline Solids. *J. Am. Ceram. Soc.* **2004**, *87*, 724−726.
(51) Thompson, T.; Yu, S.; Williams, L.; Schmidt, R. D.; Garcia-Mendez, R.; Wolfenstine, J.; Allen, J. L.; Kioupakis, E.; Siegel, D. J.; Sakamoto, J. Electrochemical Window of the Li-Ion Solid Electrolyte $Li_7La_3Zr_2O_{12}$. *ACS Energy Lett.* **2017**, *2*, 462−468.
(52) Canepa, P.; Dawson, J. A.; Sai Gautam, G.; Statham, J. M.; Parker, S. C.; Islam, M. S. Particle Morphology and Lithium Segregation to Surfaces of the $Li_7La_3Zr_2O_{12}$ Solid Electrolyte. *Chem. Mater.* **2018**, *30*, 3019−3027.
(53) Plimpton, S. Fast Parallel Algorithms for Short-Range Molecular Dynamics. *J. Comput. Phys.* **1995**, *117*, 1−19.
(54) Adams, S.; Rao, R. P. Ion Transport and Phase Transition in $Li_{7-x}La_3(Zr_{2-x}M_x)O_{12}$ (M = Ta^{5+}, Nb^{5+}, x = 0, 0.25). *J. Mater. Chem.* **2012**, *22*, 1426−1434.
(55) Klenk, M. J.; Lai, W. Finite-Size Effects on the Molecular Dynamics Simulation of Fast-Ion Conductors: A Case Study of Lithium Garnet Oxide $Li_7La_3Zr_2O_{12}$. *Solid State Ionics* **2016**, *289*, 143−149.
(56) Jalem, R.; Rushton, M. J. D.; Manalastas, W.; Nakayama, M.; Kasuga, T.; Kilner, J. A.; Grimes, R. W. Effects of Gallium Doping in Garnet-Type $Li_7La_3Zr_2O_{12}$ Solid Electrolytes. *Chem. Mater.* **2015**, *27*, 2821−2831.
(57) Ni, J.; Case, E.; Sakamoto, J.; Rangasamy, E.; Wolfenstine, J. Room Temperature Elastic Moduli and Vickers Hardness of Hot-Pressed LLZO Cubic Garnet. *J. Mater. Sci.* **2012**, *47*, 7978−7985.
(58) de Jong, M.; Chen, W.; Angsten, T.; Jain, A.; Notestine, R.; Gamst, A.; Sluiter, M.; Krishna Ande, C.; van der Zwaag, S.; Plata, J. J.; Toher, C.; Curtarolo, S.; Ceder, G.; Persson, K. A.; Asta, M. Charting the Complete Elastic Properties of Inorganic Crystalline Compounds. *Sci. Data* **2015**, *2*, No. 150009.
(59) Frenkel, D.; Smit, B. *Understanding Molecular Simulation: From Algorithms to Applications*; Academic Press, 2001.
(60) Li, Y.; Wang, Z.; Li, C.; Cao, Y.; Guo, X. Densification and Ionic-Conduction Improvement of Lithium Garnet Solid Electrolytes by Flowing Oxygen Sintering. *J. Power Sources* **2014**, *248*, 642−646.
(61) Jin, Y.; McGinn, P. J. Al-doped $Li_7La_3Zr_2O_{12}$ Synthesized by a Polymerized Complex Method. *J. Power Sources* **2011**, *196*, 8683−8687.
(62) Li, Y.; Han, J.-T.; Wang, C.-A.; Xie, H.; Goodenough, J. B. Optimizing Li^+ conductivity in a garnet framework. *J. Mater. Chem.* **2012**, *22*, 15357−15361.
(63) Cheng, L.; Park, J. S.; Hou, H.; Zorba, V.; Chen, G.; Richardson, T.; Cabana, J.; Russo, R.; Doeff, M. Effect of Microstructure and Surface Impurity Segregation on the Electrical and Electrochemical Properties of Dense Al-Substituted $Li_7La_3Zr_2O_{12}$. *J. Mater. Chem. A* **2014**, *2*, 172−181.
(64) Ren, Y.; Deng, H.; Chen, R.; Shen, Y.; Lin, Y.; Nan, C.-W. Effects of Li Source on Microstructure and Ionic Conductivity of Al-Contained $Li_{6.75}La_3Zr_{1.75}Ta_{0.25}O_{12}$ Ceramics. *J. Eur. Ceram. Soc.* **2015**, *35*, 561−572.
(65) Liu, K.; Ma, J.-T.; Wang, C.-A. Excess Lithium Salt Functions more than Compensating for Lithium Loss when Synthesizing $Li_{6.5}La_3Ta_{0.5}Zr_{1.5}O_{12}$ in Alumina Crucible. *J. Power Sources* **2014**, *260*, 109−114.
(66) Li, Y.; Cao, Y.; Guo, X. Influence of Lithium Oxide Additives on Densification and Ionic Conductivity of Garnet-Type $Li_{6.75}La_3Zr_{1.75}Ta_{0.25}O_{12}$ Solid Electrolytes. *Solid State Ionics* **2013**, *253*, 76−80.
(67) El-Shinawi, H.; Paterson, G. W.; MacLaren, D. A.; Cussen, E. J.; Corr, S. A. Low-Temperature Densification of Al-Doped $Li_7La_3Zr_2O_{12}$: a Reliable and Controllable Synthesis of Fast-Ion Conducting Garnets. *J. Mater. Chem. A* **2017**, *5*, 319−329.

DOI: 10.1021/acsami.8b17223
ACS Appl. Mater. Interfaces 2018, 10, 38151−38158